Petroleum Science 23 (2026) 4349–4363

Contents lists available at ScienceDirect

Petroleum Science

journal homepage: www.keaipublishing.com/en/journals/petroleum-science

Original Paper

Experimental study on the droplet breakup process in contracted pore throat microchannels

Yan Li [a,1], Yu-Qi Yang [a,*,1], Essouma E. Ariane F.B. [b], Xiu-Fu Cheng [c], Hai-Peng Zhang [a], Zi-Zhen Wang [a], Shu-Xing Mei [a], Jian Liu [a,**], Yue-Qun Fu [d], Si-Yu Chen [e]

[a] Engineering College, China University of Petroleum-Beijing at Karamay, Karamay, 834000, Xinjiang, China
[b] Institute of Unconventional Oil and Gas Science and Technology, China University of Petroleum (Beijing), Beijing, 102249, China
[c] College of Mechanical Engineering and Transportation, China University of Petroleum (Beijing), Beijing, 102249, China
[d] PoreLab, The Njord Centre, Department of Physics, University of Oslo, Oslo, 0371, Norway
[e] Xinjiang Special Equipment Inspection Technology Research Institute Co., Ltd, Urumqi, 830013, Xinjiang, China

ARTICLE INFO

Article history:
Received 11 April 2025
Received in revised form
8 September 2025
Accepted 7 January 2026
Available online 13 January 2026

Edited by Min Li

Keywords:
Microchannels
Pore throat
Micro-PIV
Breakup dynamics
Oil transport

ABSTRACT

This paper mainly studies the droplet breaking behavior in contracted pore throat microchannels. The droplet breaking process consists of four stages: extrusion, stretching, sub-droplet growth and fracture. The effects of interfacial tension and dispersed phase viscosity on droplet rupture were investigated. And changes in the localized pressure drop during droplet breaking. In order to understand the droplet deformation mechanism more deeply, we have successfully used micro-particle image velocimetry (micro-PIV) to describe the velocity distribution in the flow. The results show that the fluid characteristics of the continuous phase dominate the droplet deformation and fragmentation in the micro-device geometry. In addition, we built a model based on Taylor's analogy to predict the size of the child droplet formed when the parent droplet is broken during deformation, and compared it with the experimental data. The predicted model and the experimental data show a satisfactory agreement in terms of approximation.

1. Introduction

Microfluidic technology has advanced rapidly over the past decades and has found widespread applications in chemical engineering, biomedicine, and petroleum recovery (Huebner et al., 2008; Lifton, 2016; Nan et al., 2024). Due to its high precision and controllability, researchers have ingeniously utilized this technology to study fluid flow characteristics in rock formations by creating micro-models that mimic porous rock layers and reservoirs (Palizdan et al., 2020; Wang et al., 2023; Gao et al., 2024; Li et al., 2024). These micro-models are of great importance for both scientific research and industrial applications, as they significantly reduce setup and testing time compared to traditional macroscopic research equipment and enhance the flexibility of running multiple screening experiments (Nghe et al., 2010; de Haas et al., 2013). In porous rock formations, capillary forces and varying degrees of wettability result in heterogeneous permeability, leading to the trapping of residual oil droplets and reduced oil recovery efficiency (Perazzo et al., 2018; Li et al., 2020; Zhao et al., 2022). Simultaneously, the interaction between oil and water in these formations generates emulsions, which are highly beneficial for enhancing oil recovery (EOR) through emulsion flooding. Consequently, droplet breakup behavior in constricted microchannels has garnered significant interest. Roof (1970) first proposed the snap-off mechanism in constricted microchannels, suggesting that when the capillary pressure at the droplet head is less than that at the neck, the neck becomes unstable and breaks off. However, this conclusion was based on neglecting droplet velocity, and it no longer holds when droplet motion cannot be ignored (Rossen et al., 2000). Wang et al. (2014) systematically analyzed the droplet breakup process in constricted microchannels using capillary pressure variation theory, finding that

* Corresponding author.
** Corresponding author.
E-mail addresses: yuqiyang@cupk.edu.cn (Y.-Q. Yang), liujian@cup.edu.cn (J. Liu).
Peer review under the responsibility of China University of Petroleum (Beijing).
[1] Co-first author (both authors contributed equally to this work).

https://doi.org/10.1016/j.petsci.2026.01.009

Nomenclature

c	Mass concentration of glycerol or sodium dodecyl sulfate, wt%
Ca_c	Capillary number, $Ca_c = \mu_c u_c/\sigma$, non-dimensional
h	Channel height, mm
l	Droplet stretch length, mm
l_0	Initial droplet length, mm
Q_c	Volumetric flow rate of continuous phase, μL/min
Q_d	Volumetric flow rate of dispersed phase, μL/min
Q_{sum}	Volumetric flow rate of main channel, μL/min, $Q_{sum} = 2Q_c + Q_d$
Re_c	Reynolds number, $Re_c = w_c u_c \rho/\mu$, non-dimensional
R_0	Sub-droplet radius, mm
R_A	Radius of axial curvature at neck, mm
R_f	Radius of radial curvature at neck, mm
R_H	Radius of front cover, mm
R_B	Radius of back cover, mm
T	Droplet breaking cycle, s
t	Crushing process time, s
T_c	Capillary time, s
u_c	Surface velocity, $m{\cdot}s^{-1}$
D	Width of main channel, mm
w_c	Width of throat channel, mm
w	Thickness of neck, mm
We	Weber number, $We = \rho_c u_c^2 l_0/\sigma$, non-dimensional
μ_c	Viscosity of continuous phase, mPa·s
μ_d	Viscosity of dispersed phase, mPa·s
σ	Interfacial tension between two phases, $mN{\cdot}m^{-1}$
ρ_c	Density of continuous phase, $kg{\cdot}m^{-3}$
ρ_d	Density of dispersed phase, $kg{\cdot}m^{-3}$
ε	Gap width between the droplet interface at the neck and the wall of the throat, mm, $\varepsilon = w_c - w$

droplet breakup is also influenced by system velocity and viscosity, rendering Roof's criterion invalid. They proposed that the breakup criterion in constricted microchannels should be based on the critical capillary number of the dispersed and continuous phases. As droplets pass through the constricted microchannel, the droplet head is forced into the constriction zone, and the liquid-liquid interface assumes a saddle shape, with sudden breakup controlled by localized capillary pressure fluctuations (Rossen et al., 2000). This unique shape facilitates droplet breakup. Liang et al. (2021) used a self-built high-precision pressure drop measurement platform to record pressure changes during droplet breakup in constricted microchannels, surprisingly finding that the pressure drop in the constriction zone aligns with capillary pressure fluctuations, further validating the feasibility of pressure drop analysis for studying droplet breakup behavior. Zou et al. (2024) categorized the droplet breakup process into shear-dominated, compression-dominated, and snap-off stages based on capillary pressure differences, discovering that droplets transition from deformation to breakup when the neck thickness falls below a critical value. These studies have significantly enriched the research strategies for droplet breakup in constricted microchannels, providing substantial insights into the underlying mechanisms.

However, droplet breakup in constricted microchannels is not only influenced by fluid properties but also heavily dependent on the geometric shape of the constriction. The most direct evidence is that the critical capillary number for droplet breakup exhibits different trends for different constriction structures (Wang et al., 2014; He et al., 2020; Li et al., 2021). Tsai and Miksis (1994) used numerical methods to show that higher curvature pore throat structures prolong droplet breakup time and yield larger daughter droplets, while larger throat gaps under the same curvature conditions prevent droplet breakup. This indicates that droplet breakup dynamics are strongly influenced by the geometric shape of the constriction. Wang et al. (2022) compared several constricted microchannels and found that microchannels where daughter droplets are not constrained by the walls produce more uniform daughter droplets, as wall constraints affect neck formation during droplet breakup. Singla et al. (2024) mapped the interface evolution of droplets under different shape parameters, revealing that more rectangular constriction shapes lead to easier droplet deformation, attributing this to the higher gap flow velocity in rectangular constrictions, which increases the viscous forces acting on the droplets and promotes breakup. Although these findings highlight the decisive role of geometric shape, existing studies have predominantly focused on artificial regular structures (e.g., rectangular, tapered), with little attention given to the semicircular pore throat structures widely found in natural porous media (Quennouz et al., 2014). Compared to other geometric shapes (e.g., rectangular, tapered), the semicircular constricted microchannel features a larger curvature structure, resulting in reduced confinement effects from the channel walls and lower gap flow velocity (Tsai and Miksis, 1994). This significantly diminishes the guiding effect of the microchannel's constriction geometry on droplet breakup (Singla et al., 2024), necessitating further research on droplet behavior in symmetric semicircular pore throat structures.

In this study, we systematically investigated droplet breakup behavior in symmetric semicircular pore throat microchannels. Our work includes examining the effects of surfactant concentration, dispersed phase viscosity, and two-phase flow rates on droplet breakup behavior, analyzing pressure drop and capillary pressure changes as droplets pass through the pore throat, and using micro-particle image velocimetry (micro-PIV) to measure the velocity fields of the dispersed and continuous phases at the pore throat. We elucidated the breakup mechanism of droplets in symmetric semicircular pore throat structures and, based on the Taylor Analogy Breakup (TAB) model (O'Rourke and Amsden, 1987), developed a mathematical model to describe droplet breakup behavior.

2. Experimental procedures and method

The microchannel device was fabricated using photolithography and soft lithography techniques (Duffy et al., 1998). A photoresist master was made using a transparent mask and then covered with polydimethylsiloxane (PDMS). After the PDMS was cured, the PDMS plate containing the microchannel was sealed with a glass slide by plasma bonding. Before sealing, the PDMS plate and the glass slide were exposed to oxygen plasma (McDonald et al., 2000). The PDMS chip is manufactured by SMIC Qiheng, PDMS microchannels were treated with oxygen plasma (Harrick Plasma, PDC-32G) at a power of 30 W and pressure of 0.2 mbar for 60 s to activate surface groups. After plasma treatment, channels were immediately incubated at 80 °C for 2 h to promote hydrophobic recovery via reorientation of surface methyl groups. Hydrophobicity was quantified using a sessile drop method (Krüss DSA100). The measured water contact angle was

110° ± 3° (mean ± SD, *n** = 5), confirming strong hydrophobicity. This value aligns with established PDMS protocols (Zhou et al., 2010). The schematic diagram of the microchannel device used in the experiment is shown in Fig. 1. The focusing structure at the front end is used to generate droplets. The width of the dispersed phase inlet channel is 0.25 mm, the width of the continuous phase inlet channel is 1 mm, the main channel width D is 2.25 mm, the symmetrical semicircular pore throat is composed of two semicircles with a radius of 1 mm, the pore throat channel width w_c is 0.25 mm, and the height of all channels h is 0.5 mm. The symmetrical semicircular pore throat is located 24.5 mm behind the focusing structure to ensure that the droplets generated by the focusing structure remain stable before reaching the pore throat. Before the experiment, the continuous phase was continuously introduced into the microchannel for more than 20 min to avoid the wetting effect of the dispersed phase.

Fig. 2 is a schematic diagram of the experimental device, which mainly consists of four parts: microchannel chip, fluid control system, image acquisition system and particle flow sheet light display system. Two micro-injection pumps (DK Infusetek) were used to inject fluid into the microchannel. The syringe was connected to the microchannel through a polyethylene tube with a diameter of 1 mm. The microfluidic device was fixed on a microscope (WMJ-9688, Shanghai Wumo Optical Instrument CO., Ltd), and a high-speed camera (Revealer-XJ1200, Zhongke Vision Co., Ltd) was used to capture images at a range of 4000 fps. Under various operating conditions, the system was stabilized for at least 5 min, and then the experimental images were recorded by a high-speed camera. The images were processed by ImageJ software, and the measurement error of the experimental data (including the length of the initial droplet l_0, the tensile length l, the radius of the sub-droplet R_0, the radius of axial curvature at the neck R_A, the radial radius of curvature at the neck R_f, the radius of the front cover R_H and the radius of the back cover R_B) was ±3%~±5%. The experiment was carried out at 293.15 ± 1 K and atmospheric pressure. The micro-PIV system can capture the velocity matrix of a large number of spatial points marked with fluorescent microspheres, providing rich spatial structure of the velocity field and flow characteristics. Studies have shown that its influence on the flow topology is negligible (Ma et al., 2015). Monodisperse polystyrene fluorescent microspheres (2 μm in diameter, 0.5 wt% added) were used as tracer particles and were purchased from Jiangsu Zhichuan Technology Co., Ltd. A concentration of 0.5 wt% fluorescent particles (2 μm diameter) was used to ensure high signal-to-noise ratio while minimizing flow disturbance. This density is below the 5 wt% threshold shown to negligibly alter fluid viscosity and flow topology (Ma et al., 2015). As cited in Ma et al. (2015), sub-2-μm particles at low concentrations do not perturb

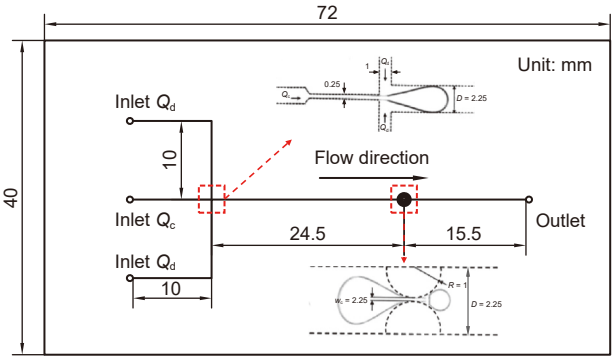

Fig. 1. Schematic diagram of microchannel structure.

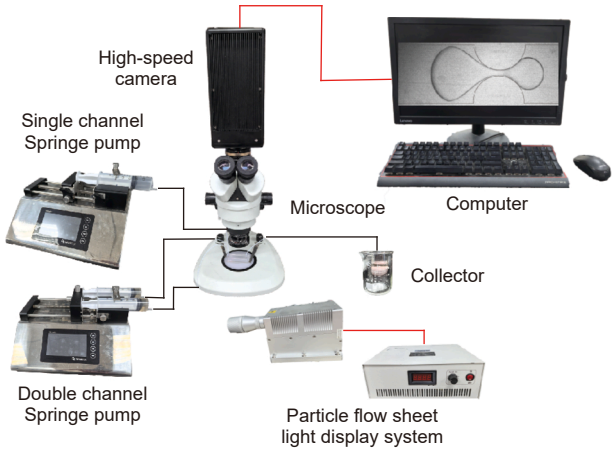

Fig. 2. Schematic diagram of the experimental setup.

microfluidic flows due to their small Stokes number ($St < 10^{-3}$). We avoid the free movement of tracer particles between the two phases during the testing process by adding hydrophobic ordinary polystyrene microspheres to mineral oil (continuous phase) and adding hydrophilic carboxylated polystyrene microspheres to water (dispersed phase) respectively. The excitation of the fluorescent microspheres was achieved by using a particle flow sheet light display system with an output power of 8 W, a wavelength of 532 nm, and a thickness of 1 mm. The fluorescent microspheres directly irradiated by the laser sheet will produce fluorescence, while the fluorescent microspheres not irradiated by the laser sheet will not emit light. In a completely dark environment, a high-speed camera (Revealer-XJ1200, 4000 frames/s) attached to the microscope objective was used to capture the movement of the fluorescent microspheres in the microchannel. The experimental images were analyzed and processed by MicroVec v3.6.2 software developed by Beijing Cube World Technology Development Co., Ltd.

In the experiment, several experimental groups with different interfacial tension used mineral oil as the continuous phase, and added different mass fractions (0.05, 0.08, 0.1, 0.12 wt%) of sodium dodecyl sulfate (SDS) aqueous solution as the dispersed phase. Different experimental groups with various viscosities used mineral oil with excessive S-pan80 (1 wt%) as the continuous phase to eliminate the influence of interfacial tension changes on the experimental results, and used glycerol aqueous solution with different mass fractions (0, 10, 15, 20 wt%) as the dispersed phase. The physical properties of the working system such as density, viscosity and interfacial tension are shown in Table 1. The density of the experimental fluids was measured using a densitometer (Anton Paar, Austria), the viscosity was measured with an automatic capillary viscometer (iVisc, LAUDA, Germany), and the interfacial tension was measured using a surface tensiometer (OCAH200, Data Physics Instruments GmbH, Germany). The flow rate ranges of the continuous phase and the dispersed phase are: $0 < Q_c \leq 260$ μL/min, and $0 < Q_d \leq 120$ μL/min, respectively. In petroleum reservoirs, interstitial flow velocities typically range from 0.1 to 10 mm/s. Our micochannel throat diameter (0.25 mm) and flow rates (10–260 μL/min) correspond to superficial velocities of 1.3–34.7 mm/s, capturing capillary-dominated (low flow) to viscous-inertial transition (high flow) regimes relevant to enhanced oil recovery (EOR) processes. Wang et al. (2014) used flow rates of 5–200 μL/min in constricted microchannels to study droplet breakup under reservoir-relevant conditions. Our upper limit (260 μL/min) extends this range to explore higher shear/

Table 1
Physical properties of the working system.

System No.	Dispersed water phase	Continuous oil phase	Water phase density, kg/m^3	Viscosity of water phase, mPa·s	Oil phase density, kg/m^3	Oil phase viscosity, mPa·s	Interfacial tension, mN/m
A	0.05 wt% SDS aqueous solution	Mineral oil	1000	0.92	845	48.60	17.96
B	0.08 wt% SDS aqueous solution	Mineral oil	1000	0.92	845	48.60	11.54
C	0.1 wt% SDS aqueous solution	Mineral oil	1000	0.92	845	48.60	8.46
D	0.12 wt% SDS aqueous solution	Mineral oil	1000	0.92	845	48.60	7.81
E	Pure water	Mineral oil (1 wt% S-pan80)	1000	0.92	845	48.60	3.54
F	10 wt% glycerol-water solution	Mineral oil (1 wt% S-pan80)	1021	1.64	845	48.60	3.04
G	15 wt% glycerol-water solution	Mineral oil (1 wt% S-pan80)	1036	2.06	845	48.60	2.84
H	20 wt% glycerol-water solution	Mineral oil (1 wt% S-pan80)	1047	2.63	845	48.60	2.4

viscous forces while maintaining $Re < 50$ (ensuring laminar flow). The Reynolds number Re_c ($Re_c = w_c u_c \rho/\mu$, where surface velocity $u_c = (2Q_c + Q_d)/(w_c \times h)$) characterizes the relative magnitude of inertial force and viscous force is 0.45–3.02; the capillary number Ca_c ($Ca_c = \mu u_c/\sigma$) characterizes the relative magnitude of viscous force and interfacial tension is 0.069–0.917. The droplet breakup process is mainly affected by squeezing stress, viscous shear stress and interfacial tension.

3. Results and discussion

3.1. Droplet breakup

3.1.1. Droplet breakup process

The droplets will deform and break as they pass through the symmetrical semicircular orifice throat along the microchannel. When a droplet enters a symmetrical semicircular pore throat, the deformation behavior of the droplet can be characterized by the evolution of the stretching length l of the droplet along the central axis. Fig. 3 shows the physical parameters in the droplet breakup process, where l_0 represents the length of the initial droplet, D is the main microchannel width, w_c is the width of the narrowest part of the symmetrical semicircular pore throat, R is the droplet radius, R_A is the axial curvature radius at the neck, R_f is the radial curvature radius at the neck, R_H is the front cover radius, and R_B is the back cover radius. In addition, T represents the cycle time of droplet breakup, and t represents the time of the droplet breakup process. Capillary time is defined as T_c, which is a measure of the time it takes for an interface to recover its shape in a low-viscosity fluid under the action of capillary forces.

When a single uniform droplet approaches a semicircular symmetrical pore throat, due to the limitation of the microchannel geometric structure, the flow velocity at the central axis of the channel increases, and the continuous phase fluid near the edge of the microchannel begins to flow toward the central axis of the channel to squeeze the droplet, causing the droplet to deform. When the front end of the droplet is about to enter the symmetric semicircular pore throat, the droplet begins to deform. The point where the front end of the droplet is located at this time is recorded as the origin z_0, and the time is recorded as $t = 0$. The moment when the droplet breaks through the pore throat to form a new droplet is taken as the end time, at which point the breakup time reaches its maximum value ($T = t_{max}$). The droplet breakup process is shown in Fig. 4.

According to the growth rate of the droplet length along the z-axis, the droplet breakup process can be divided into four stages: squeezing, stretching, sub-droplet growth and snap-off stages (Du et al., 2018), as shown in Fig. 5.

I. Squeezing stage ($t < t_1$): due to the limitation of the microchannel pore throat geometry, the droplet is continuously squeezed, and the front end of the droplet begins to deform. The shape of the front end of the droplet adapts to the pore throat structure, forming a protruding tip, which

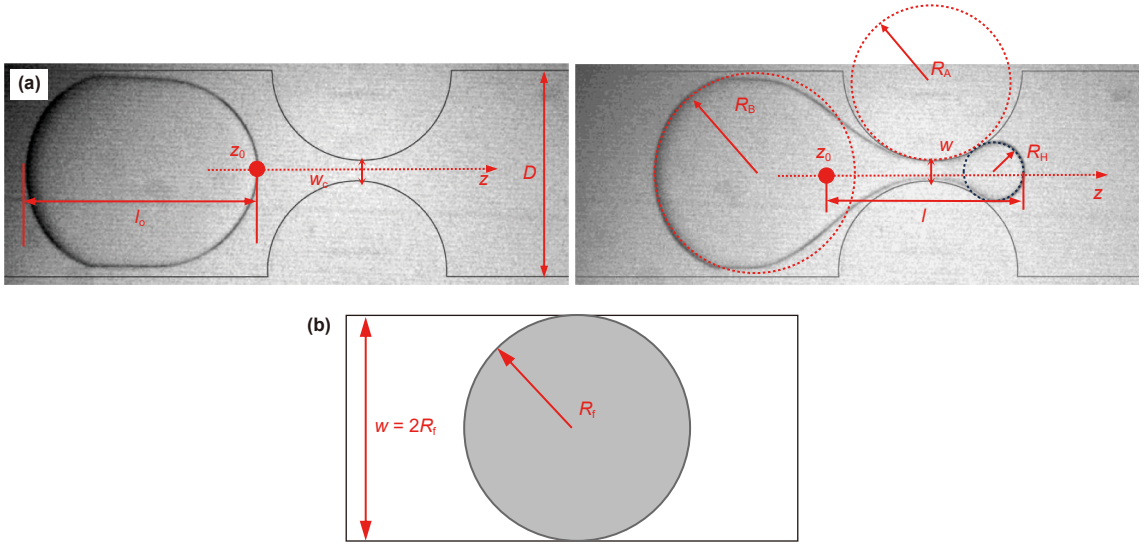

Fig. 3. **(a)** Schematic diagram of physical parameters during droplet breakup; **(b)** Schematic diagram of the vertical cross-section of the neck at the narrowest part of the pore throat.

continues to grow until it fits with the semicircular symmetrical pore throat, and the droplet completely occupies the entrance of the pore throat channel, as shown in Fig. 4.

II. Stretching stage ($t_1 \leq t < t_2$): after the droplet completely occupies the pore throat entrance, the width of the pore throat channel at the front of the droplet decreases sharply, the squeezing effect on the droplet increases sharply, the tip of the droplet thins rapidly in the direction perpendicular to the *z*-axis, and stretches along the channel. This stage is the stage where the droplet length changes fastest along the *z*-axis during the droplet breakup process, as shown in Fig. 5(a).

III. Sub-droplet growth stage ($t_2 \leq t < t_3$): the tip of the droplet passes through the pore throat channel and grows downstream of the pore throat, forming a dumbbell shape. At this time, the droplet forms a neck at the pore throat channel (as shown in Fig. 4). The position of the line connecting the centers of the two semicircles of the pore throat is the neck thickness *w*. Due to the gap between the droplet and the microchannel wall, the neck thickness *w* is slightly smaller than the narrowest width w_c of the semicircular symmetrical pore throat. The squeezing pressure of the droplet at the upstream end of the pore throat is relatively large, and the droplet at the downstream end of the pore throat continues to grow. During this process, the neck thickness remains basically unchanged, as shown in Fig. 6.

IV. Snap-off stage ($t > t_3$): Under the restriction of the symmetric semicircular pore throat structure, the droplet is blocked at the pore throat. The upstream continuous phase applies pressure to the droplet, creating a Laplace pressure difference between the high-curvature neck and the low-curvature sub-droplet. This pressure imbalance drives rapid thinning of the neck, culminating in snap-off. The neck thickness decreases drastically during this process, as shown in Fig. 6.

3.1.2. Effect of interfacial tension

Interfacial tension is an important factor affecting the breakup process of droplets passing through pore throats. In the experiment, the interfacial tension of the oil-water interface was changed by adding different mass fractions of SDS to water. Fig. 5(d) shows the evolution of droplet length under different interfacial tensions. Under the same two-phase flow rate, the time of each stage of the droplet breakup process tends to decrease significantly with the decrease of interfacial tension, and the dimensionless length growth rate of the droplet also decreases with the decrease of interfacial tension, as shown in Fig. 5(c). Obviously, the breakup period of the droplet is not only affected by the interfacial tension, but also by the two-phase flow rate. With the increase of the continuous phase flow rate, the droplet obtains a greater driving force, allowing the droplet to pass through the pore throat at a faster velocity. The most obvious performance is that the growth rate of the dimensionless length in the stretching stage increases faster, as shown in Fig. 5(a). In order to verify this judgment, we analyzed and compared the time of each stage of droplet breakup under different continuous phase flow rates and different interfacial tension conditions in detail. As shown in Fig. 7(a)–(d).

As the dispersed phase flow rate increases, the time required for the squeezing stage gradually decreases, but the time proportion does not change much. Due to the obstruction of the pore throat channel geometry, the filling velocity along the *z*-axis direction after entering the pore throat channel is accelerated. The increase in the dispersed phase flow rate strengthens this effect, making the front end of the droplet enter the pore throat channel faster and more susceptible to the sheer force of the continuous phase. The time proportion of the sub-droplet growth stage decreases with the increase of the dispersed phase flow rate, which means that the droplet grows faster and reaches the pinch-off stage earlier. With the increase of SDS concentration, the interfacial tension between the dispersed phase and the continuous phase continues to decrease, the anti-interference ability of the droplet interface is weakened, the deformation of the interface shape is more susceptible to the sheer force of the continuous phase, and the duration of each stage of droplet breakup is reduced. The most obvious changes are in the sub-droplet growth stage and the snap-off stage. Due to the reduction of interfacial tension, the particle size of the sub-droplet produced by droplet breakup becomes smaller and smaller, which reduces the duration of the sub-droplet growth stage, as shown in Fig. 7(b). In the

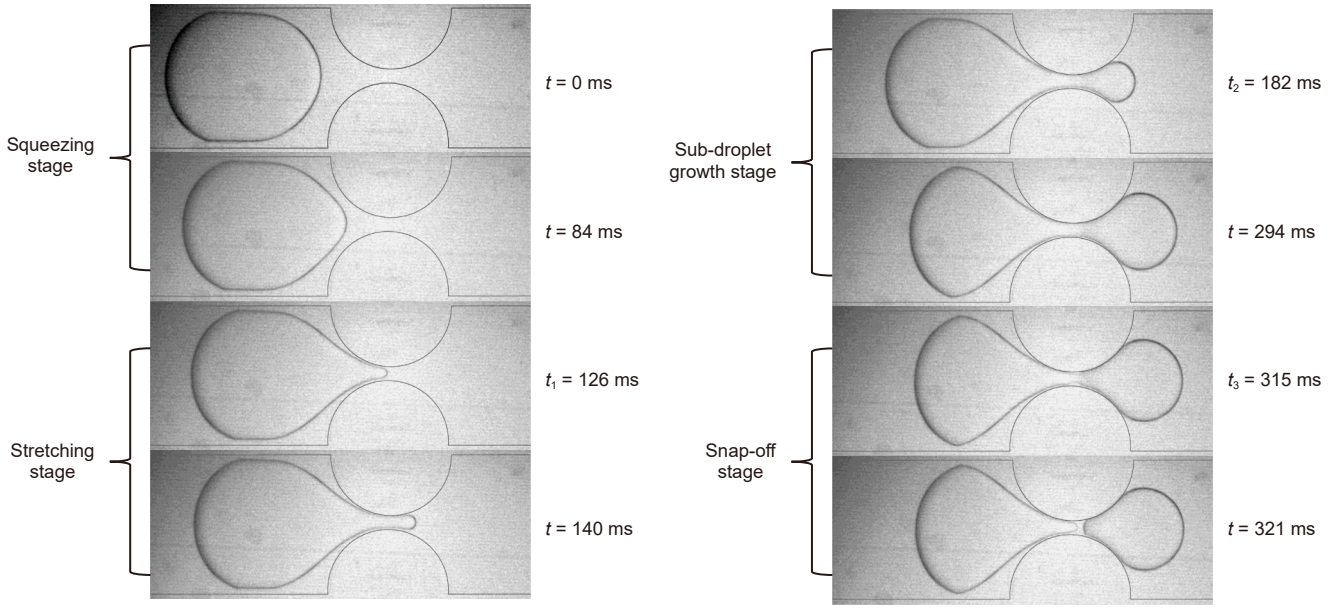

Fig. 4. The droplet breakup process in the symmetric semicircular pore throat channel: *c* (SDS) = 0.05 wt%, Q_c = 50 μL/min, Q_d = 100 μL/min.

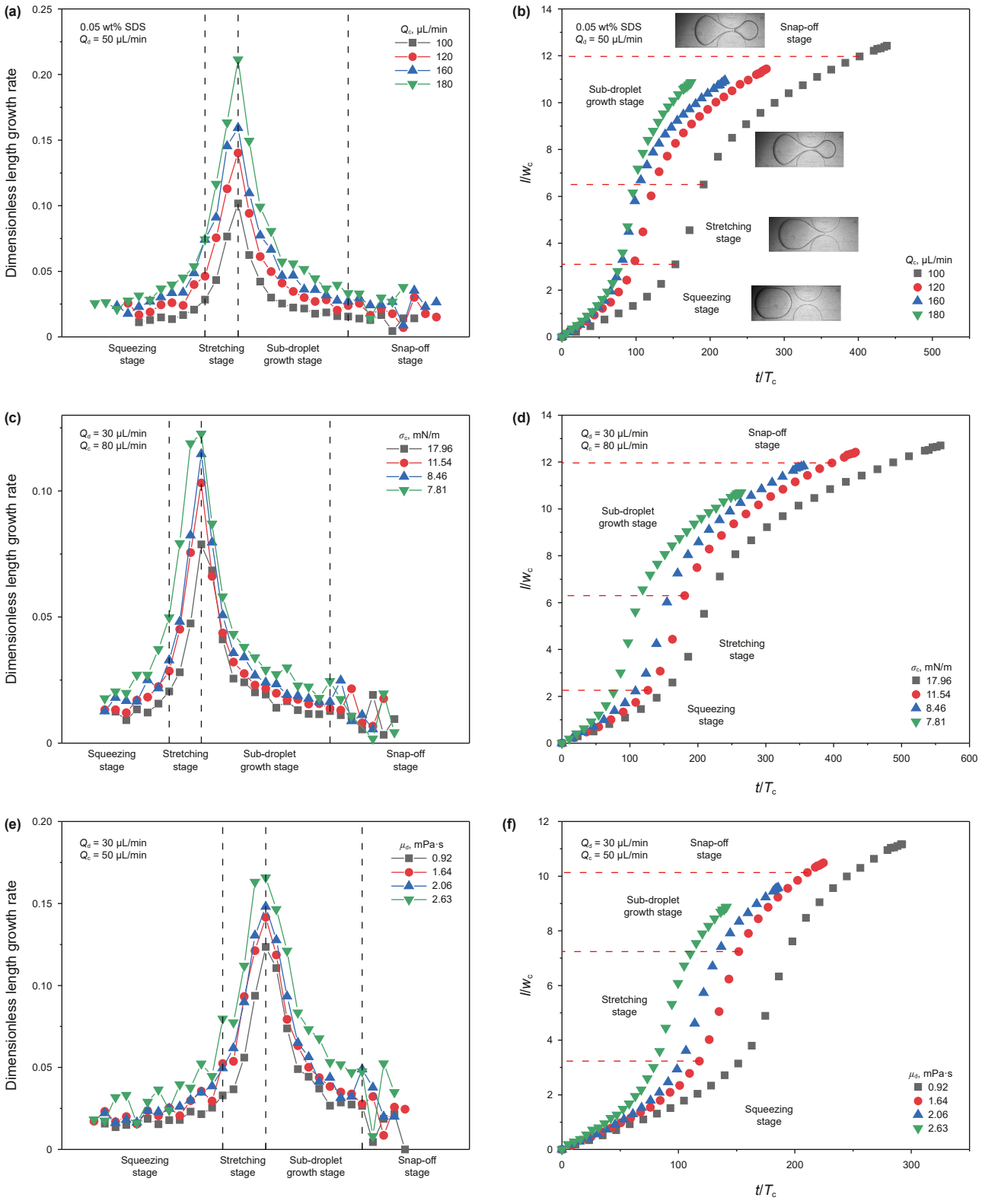

Fig. 5. **(a)** Dimensionless length growth rate under different continuous phase flow conditions; **(b)** Evolution of dimensionless length l/w_c with dimensionless time t/T_c under different continuous phase flow conditions; **(c)** Dimensionless length growth rate under different interfacial tension conditions; **(d)** Evolution of dimensionless length l/w_c with dimensionless time t/T_c under different interfacial tension conditions; **(e)** Dimensionless length growth rate under different dispersed phase viscosities; **(f)** Evolution of dimensionless length l/w_c with dimensionless time t/T_c under different dispersed phase viscosities.

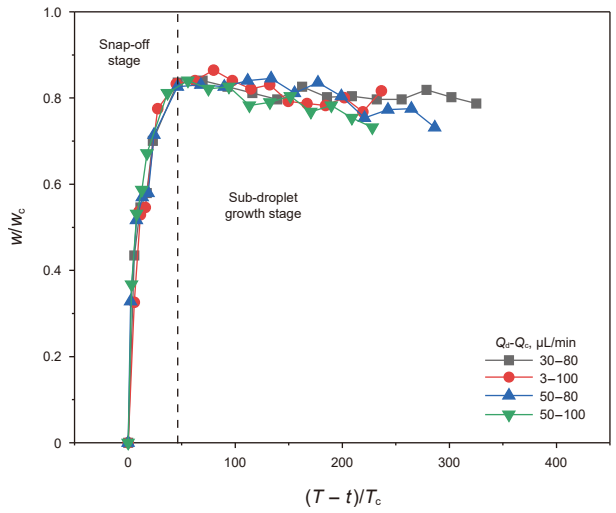

Fig. 6. Evolution of the dimensionless width w/w_c as a function of the dimensionless time $(T-t)/T_c$. c (SDS) = 0.05 wt%.

snap-off stage, due to the increase in SDS concentration, the surfactant concentration gradient at the neck break diminishes under the same working conditions. This reduces the Marangoni stress, which would otherwise counteract interfacial perturbations. Consequently, the damping effect on capillary pressure fluctuations is weakened. As a result, once a depression forms at the neck, the snap-off process of the droplet becomes more intense.

In order to further eliminate the influence caused by the length difference of the mother liquid droplets under different working conditions, the ratio of each stage time to the crushing cycle is shown in Fig. 7(c). The increase in the continuous phase flow rate has the most significant impact on the sub-droplet growth stage. Larger continuous phase flow rate provides a greater driving force for the droplets, causing the droplets to occupy a much smaller proportion of the time in the sub-droplet growth stage. In Fig. 7(d), the time proportion of the sub-droplet growth stage begins to decrease as the interfacial tension decreases, which coincides with the decrease in the sub-droplet size (Fig. 7(b)).

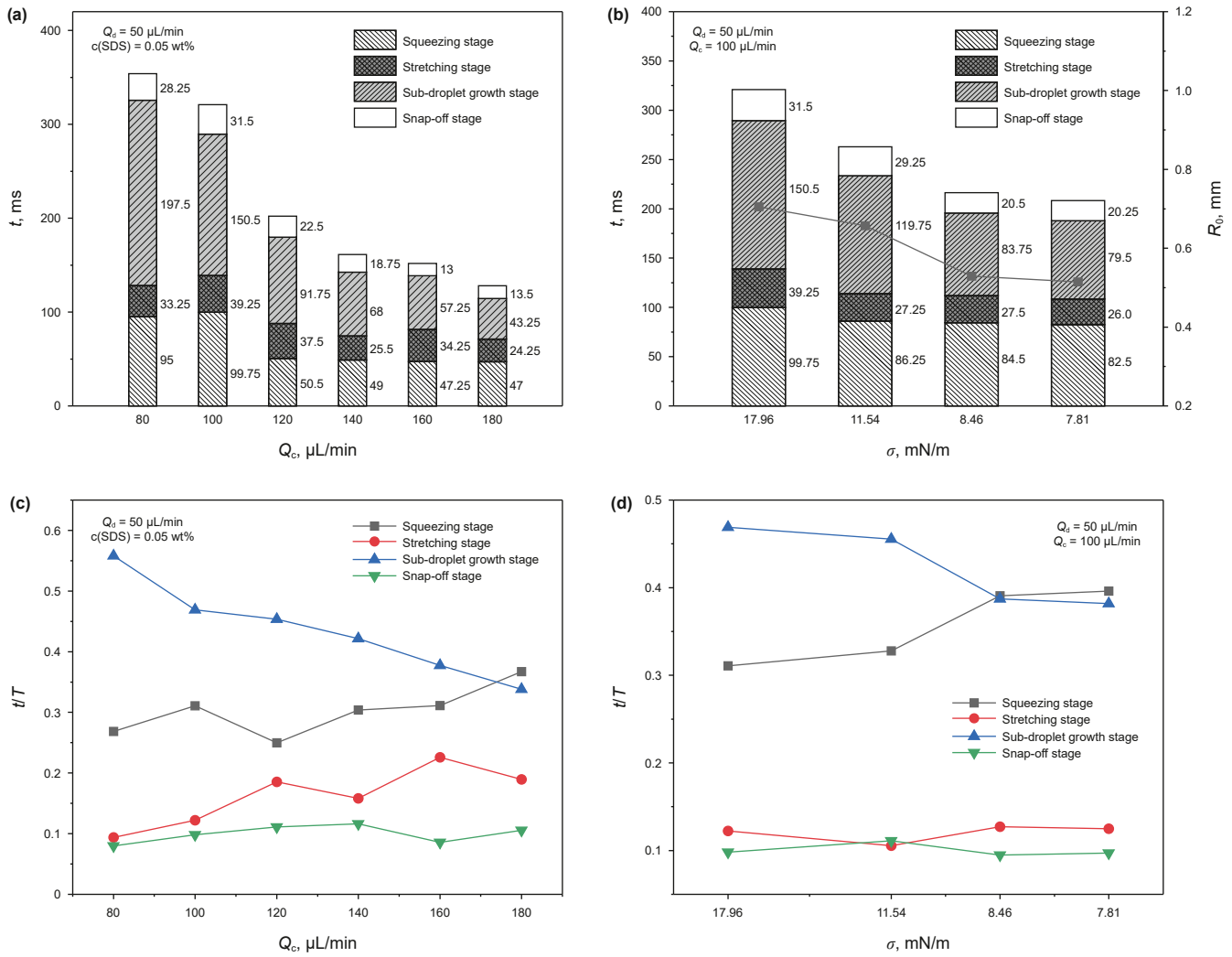

Fig. 7. **(a)** Time of each stage of droplet breakup under different continuous phase flow conditions; **(b)** Time of each stage of droplet breakup under different interfacial tension conditions; **(c)** Time proportion of each stage of droplet breakup in the rupture cycle under different continuous phase flow conditions; **(d)** Time proportion of each stage of droplet breakup in the rupture cycle under different interfacial tension conditions.

3.1.3. Effect of dispersed phase viscosity

Viscous force is one of the main factors that dominate droplet breakup. We changed the viscosity of the dispersed phase by adding different mass fractions of glycerol to the water phase. Although the viscosity of the dispersed phase varies within a small range (0.92–2.63 mPa·s), higher viscosity increases the resistance to interfacial deformation, making it more difficult to initiate droplet breakup under the same flow conditions. Droplets that would otherwise break at lower viscosities only deform without fracturing. The contribution made by the increase in the continuous phase flow rate in the different viscosity experimental groups is the same as that in the different interfacial tension groups, which reduces the time proportion of the sub-droplet growth stage, but the difference is that the time proportion of the squeezing stage is increased, so that the time spent in the squeezing stage at a higher continuous phase flow rate contributes more to the breakup cycle, as shown in Fig. 8(a) and (c). After increasing the viscosity of the dispersed phase, the time proportion of the squeezing stage becomes the main part of the breakup cycle, and this proportion continues to increase with the increase of the continuous phase flow rate. Obviously, due to the small difference in the viscosity of the dispersed phase, the viscosity change has little effect on the time proportion of each stage of droplet breakup, as shown in Fig. 8(d).

Tsai and Miksis (1994) used the Stokes equation to show the relationship between the bubble breakup mechanism and the viscosity ratio in the contraction structure. The smaller the viscosity ratio of the dispersed phase to the continuous phase, the longer the bubble pinch-off time and the larger the particle size of the sub-droplet. According to experimental observations, the droplet breakup mechanism in the contraction structure also has a similar relationship. Once breakup is initiated, higher dispersed phase viscosity accelerates the necking process, leading to a significantly reduced snap-off stage time, as shown in Fig. 8(b). Although there are differences in the properties of gas and liquid, the liquid itself has an internal viscosity, while the internal viscosity of the gas is so small that it can be almost ignored. However, their breakup mechanisms in the contraction structure microchannel have certain commonalities.

Unfortunately, Wang et al. (2014) obtained the opposite conclusion from the above conclusions when the breakup time changes with Ca under different viscosity ratios. This may be caused by the microchannel geometry. The sudden contraction structure used by Wang has a strong restriction effect on the flow of the continuous phase at the contraction, while Tsai and we used a circular contraction structure with a large curvature, which makes the dispersed phase flow faster downstream along the contraction and the gap between the droplets during the breakup process, and ultimately leads to a shorter breakup time and a smaller droplet size.

3.2. Local pressure drop at the orifice

Since the droplet will hinder the flow of the continuous phase when entering the pore throat, this will increase the pressure upstream of the pore throat, and the squeezing force has an important influence on the droplet breakup process. To further understand the droplet breakup mechanism, we investigate the localized pressure drop changes at the symmetric semicircular pore throat during the droplet breakup process. The change in the droplet neck thickness after the droplet enters the pore throat channel is shown in Fig. 6. We found that the gap width ($\varepsilon = w_c - w$) between the neck interface and the pore throat wall during the growth stage of the sub-droplet $\varepsilon \ll w_c$. This means that the droplet passing through the pore throat does not completely contact the microchannel wall, and there is a gap flow between the two. Therefore, we can use the film lubrication theory to further study the droplet breakup. According to the lubrication theory analysis, due to the hydrophobic properties of the microchannel material, the droplet does not completely contact the channel wall when the dispersed phase passes through the pore throat and is driven by pressure. The continuous phase forms a liquid film at the droplet and the microchannel wall to provide lubrication for the droplet flow deformation. Based on the film lubrication theory, Stone obtained the analytical solution of the driving pressure drop of the droplet when passing through the saddle-shaped micro-contraction channel with respect to the Stokes equation. The model incorporates elements of it to approximate flow in the thin gap between the droplet and the throat wall, and extends lubrication theory by accounting for transient necking effects via a time-dependent curvature term ($(R_A/R_f)^{1/2}$). The geometric model of the "saddle-shaped" channel structure established by this model is highly compatible with the geometric shape of the symmetric semicircular orifice throat. When a droplet passes through a saddle-shaped micro-contraction channel, the pressure drop in the upstream and downstream of the channel is given by Eq. (1) (Stone, 2005). However, since the physical model of the droplet is based on the channel structure, this equation cannot analyze the driving pressure drop before the droplet completely enters the pore throat, that is, it cannot analyze the driving pressure in the squeezing stage and the stretching stage.

$$\frac{12\mu Q}{(w_c/2)^3 \Delta P}\left(\frac{R_A}{R_f}\right)^{1/2} = \frac{6}{7} \Rightarrow \Delta P_{drive} = \frac{14\mu Q_{sum}}{(w_c/2)^3}\left(\frac{R_A}{R_f}\right)^{1/2} \tag{1}$$

The results are shown in Fig. 9. Under the shearing action of the continuous phase, the front end of the droplet enters the pore throat channel to form a "dumbbell shape", resulting in uneven pressure distribution upstream and downstream in the microchannel. At this time, the pressure of the upstream continuous phase becomes the driving force to make the sub-droplet grow slowly. During the sub-droplet growth stage, the driving pressure drop always remains at a small stable value until the thickness of the droplet neck begins to thin, and the pressure drop increases rapidly. After the droplet is broken, the driving pressure drop decreases again. The droplet completes the change in the peak pressure drop during the pinch-off stage. Liang et al. also found that the droplet breakup time node coincided with the peak pressure drop when using a micro-pressure sensor to measure the pressure drop of a droplet passing through a micro-contraction channel. (Liang et al., 2021). Obviously, the breakup of droplets in a contraction-type microchannel is often accompanied by a dramatic change in pressure drop. By analyzing the change in pressure drop in the microchannel, the breakup of droplets can be effectively predicted.

At the same time, we also further studied the dynamic breakup process of the droplet when it passes through the pore throat. The change of the local pressure of the droplet and the change of the interface at the neck, head and tail of the droplet are given by the Young-Laplace Eqs. (2)–(4):

$$\Delta P_N = \gamma\left(\frac{1}{R_f} - \frac{1}{R_A}\right) \tag{2}$$

$$\Delta P_H = \frac{2\gamma}{R_H} \tag{3}$$

$$\Delta P_B = \frac{2\gamma}{R_B} \tag{4}$$

Roof (1970) proposed in his study the static breakup criterion for the breakup of droplets in a contraction-type microchannel

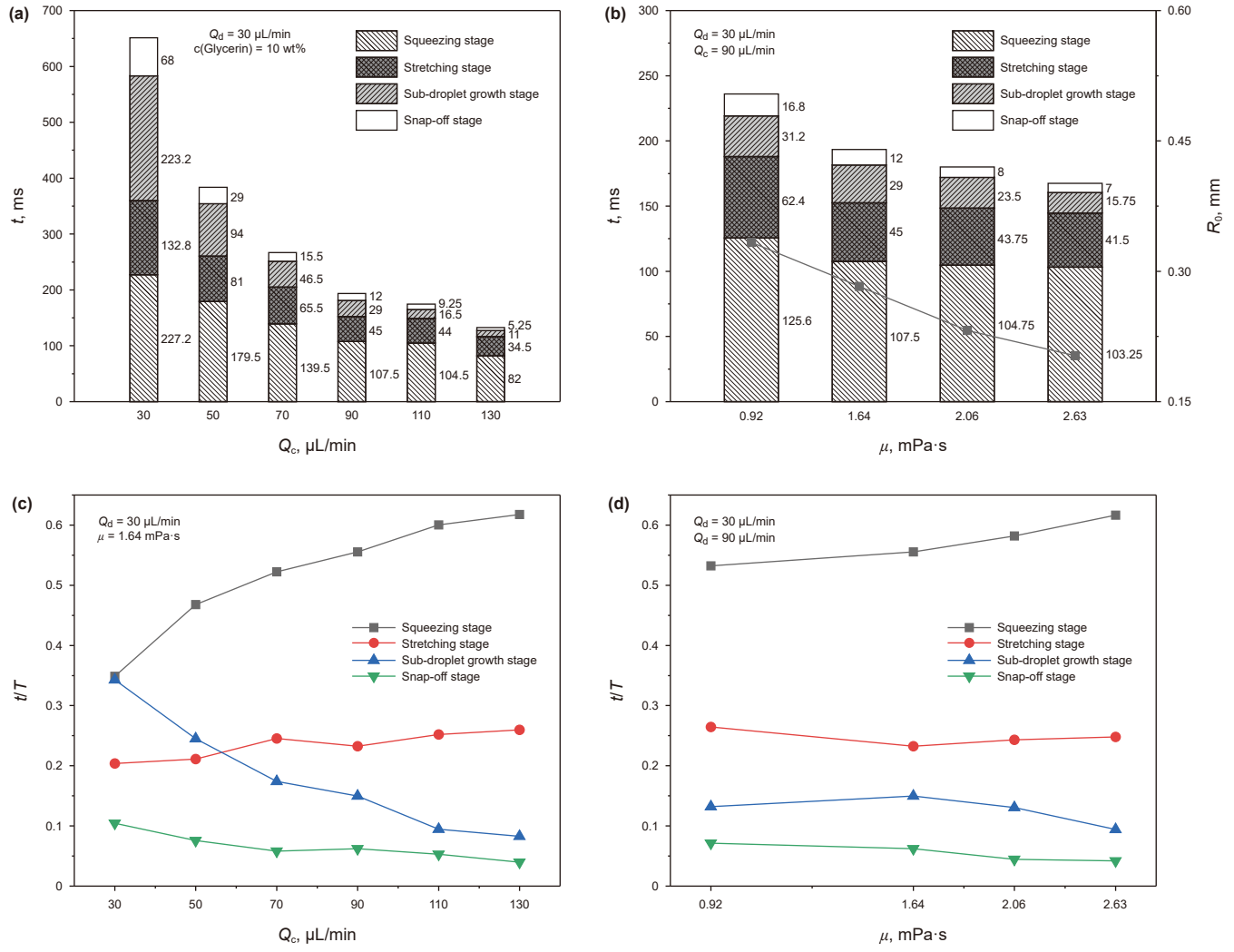

Fig. 8. **(a)** The time of each stage of droplet breakup under different continuous phase flow conditions; **(b)** The time of each stage of droplet breakup under different viscosity conditions; **(c)** The proportion of the time of each stage of droplet breakup in the rupture cycle under different continuous phase flow conditions; **(d)** The proportion of the time of each stage of droplet breakup in the rupture cycle under different viscosity conditions.

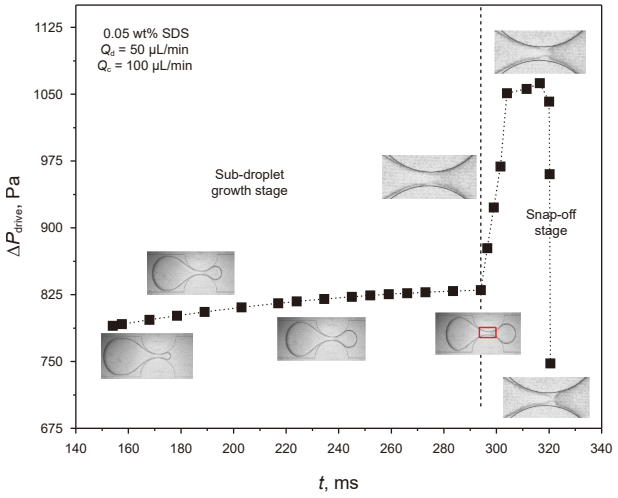

Fig. 9. Driving pressure drop.

when the capillary pressures at the head and neck of the droplet are equal. However, his research conclusion was made under extremely low flow rate conditions. Obviously, when the two-phase flow rate increases, it will cause greater flow resistance, and the judgment of this criterion will have a large deviation. The pressure difference between the head and tail and the neck is given by Eqs. (5) and (6): (Wang et al., 2022):

$$P_H - P_N = \Delta P_N - \Delta P_H \tag{5}$$

$$P_B - P_N = \Delta P_N - \Delta P_B \tag{6}$$

Fig. 10 shows the change of pressure difference between the head and tail and the neck during the growth and snap-off stages of the sub-droplet. We found that the pressure difference of the tail was significantly greater than the pressure difference of the head in the early stage of the growth of the sub-droplet, and the pressure difference between the head and the neck was negative. This means that the capillary pressure of the droplet in the pore throat is much greater than the capillary pressure of the droplet

head at this time, which well explains the rapid deformation of the droplet head when passing through the pore throat clamp during the stretching stage. The squeezing effect of the continuous phase on the dispersed phase is the dominant factor in the growth of the sub-droplet, and the imbalance of the pressure between the head and the tail provides the driving force for the growth of the sub-droplet. After entering the snap-off stage, the pressure imbalance of the head and tail of the droplet is further weakened, but the pressure difference between the head and the tail and the neck is positive. Obviously, the static breakup criterion proposed by Roof is not applicable to the droplet breakup under this condition (Roof, 1970). The pressure difference increases rapidly when the droplet breaks up. We speculate that after the droplets grow to a certain size, the Laplace pressure jump will occur along with the breakup of the droplets due to the influence of Rayleigh - Plateau instability, prompting the droplets to break up. Wang et al. (2022) also observed a similar phenomenon in their study of square micro-contraction channels.

3.3. Micro-PIV analysis

The micro-Particle Image Velocimetry technique (micro-PIV) was used to analyze the velocity field distribution of the continuous phase during the breakup process of the droplet passing through the pore throat, as shown in Fig. 11. In Fig. 11(a), it can be clearly observed that due to the existence of the symmetric semicircular pore throat, the flow velocity of the continuous phase through the pore throat increases significantly when the droplet does not contact the pore throat. As the droplet gets closer and closer to the pore throat, although the droplet has not entered the pore throat, it is affected by the velocity field of the continuous phase, and the front end of the droplet begins to deform and enter the squeezing stage (Fig. 11(b)). When the front end of the droplet enters the pore throat, the flow of the continuous phase at the pore throat is blocked (Fig. 10(c)), and the kinetic potential energy of the continuous phase is further converted into the driving pressure of the droplet passing through the pore throat (Abate et al., 2012). Under the driving pressure caused by the continuous phase and the capillary force, the front end of the droplet passes through the pore throat in a very short time, and the droplet is deformed into a “dumbbell shape” (Fig. 11(d)). After entering the sub-droplet growth stage, the continuous phase only flows downstream through the gap between the droplet neck and the pore throat to form interstitial flow (Wong et al., 1995). The existence of interstitial flow further strengthens the shearing effect of the continuous phase on the droplet. Under the squeezing effect of the driving pressure of the upstream continuous phase and the shearing effect of the interstitial flow, the downstream end of the “dumbbell-shaped” droplet continues to grow, further hindering the flow of the interstitial flow downstream, and the droplet driving pressure drop increases (Fig. 9), which increases the interstitial flow velocity (Fig. 11(e)). The shearing effect of the interstitial flow on the interface at the droplet neck is enhanced, and the balance between shear force and interfacial tension is broken. At this time, the shear force dominates ($Ca_c > 0.01$) (Yao et al., 2021), the interface at the neck of the “dumbbell-shaped” droplet is deformed, the neck thickness rapidly decreases (Fig. 6), and finally the neck breaks to form a new sub-droplet (Fig. 11(e), $t = 152$ ms).

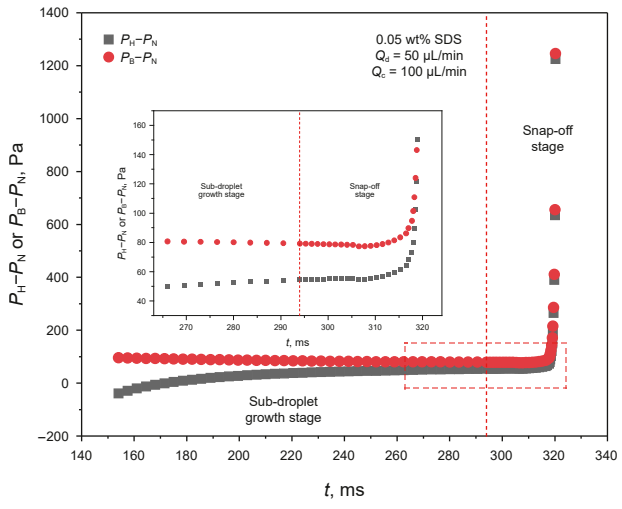

Fig. 10. Changes in pressure difference between the head, tail and neck.

When the front end of the droplet first enters the pore throat, the symmetric semicircular structure with large curvature does not damage the interface of the droplet, and the droplet deforms along the channel wall to form a “dumbbell shape”. However, the gap flow formed between the droplet and the channel wall during the growth of the sub-droplet cannot be ignored for the further evolution of the droplet. As shown in Fig. 9, the driving pressure drop of the droplet does not change significantly during the sub-droplet growth stage, which corresponds exactly to Fig. 11(d). During the sub-droplet growth stage, the velocity field distribution of the continuous phase at the pore throat maintains a uniformly distributed small velocity. At this time, the effect of the gap flow on the droplet is only to rely on the viscous shear force and the driving pressure of the upstream continuous phase to promote the further growth of the sub-droplet.

We also observed the velocity field distribution inside the droplet under higher capillary number conditions, as shown in Fig. 12. Before the droplet deforms, the interior of the droplet maintains a higher velocity (Fig. 12(a)). When the droplet begins to deform, high velocity field begins to move toward the droplet front, as shown in Fig. 12(b) and (c). Interestingly, after the droplet is deformed into a “dumbbell shape”, the velocity field inside the downstream end of the droplet is significantly higher than that at the neck, as shown in Fig. 12(d). After the sub-droplet is formed, the velocity field distribution inside the sub-droplet maintains the same distribution rule as the mother droplet, and the internal velocity is always higher than the edge, as shown in Fig. 12(e).

3.4. Droplet size

As a droplet passes through a symmetric semicircular pore-throat channel, its shape and size change due to various factors. These factors include the force exerted by the continuous phase fluid, the change in the internal pressure of the droplet, the physical properties of the fluid (such as surface tension, capillary number and viscosity ratio), and the size and geometry of the microchannel. During the deformation and fragmentation process, the bubble stretches, resulting in an increase in its total length along the z-axis, while the its neck width also changes. The deformation and fragmentation process leads to the generation of a new sub-droplet with a specific radius (O'Rourke and Amsden, 1987) best represents the combined fluid interactions that lead to the oscillation, deformation and fragmentation of the parent bubble. The analogy theory is based on the oscillation and translation of the droplet, which is affected by the continuous flow field of the continuous phase liquid and the system consisting of viscosity and mass. The interfacial tension as well as the viscous forces of the continuous phase fluid play a key role in this flow situation. Therefore, there is a separation between the total length of the elongated droplet and the flow inside the narrow part. The increase in tensile stress mainly starts only in the contraction region, ignoring the effects of gravity

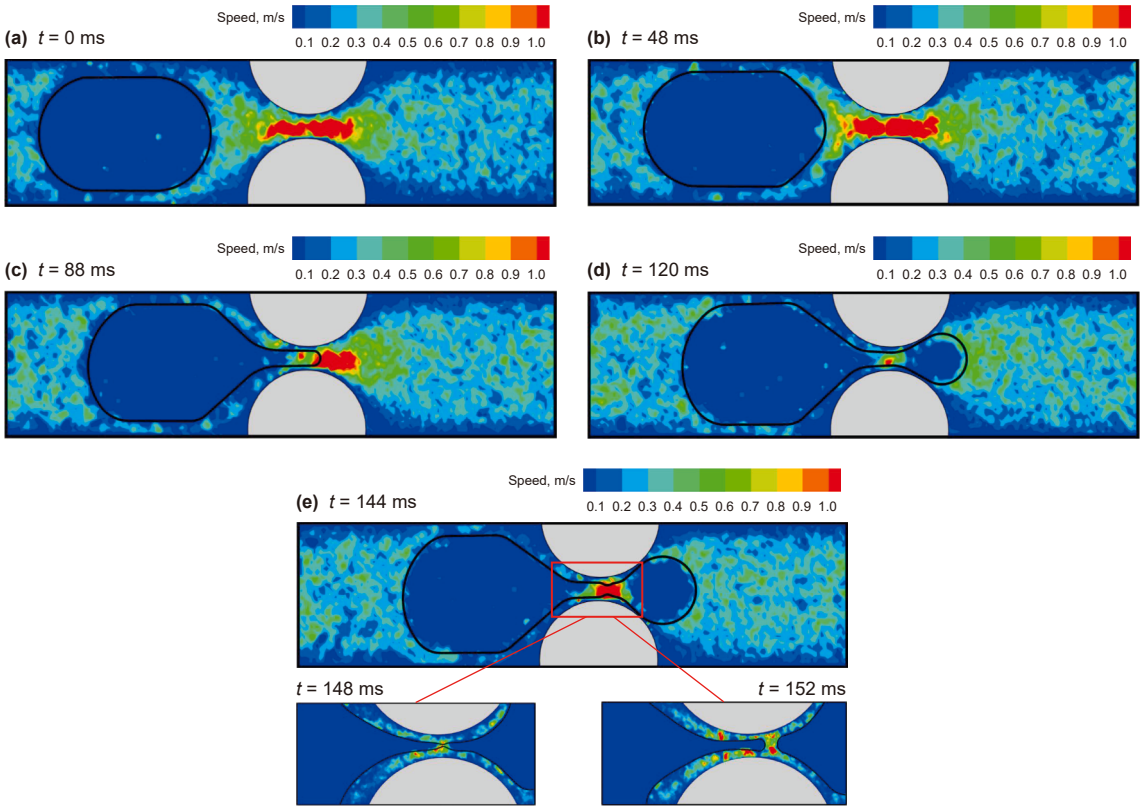

Fig. 11. Micro-PIV analysis of the velocity field distribution of the continuous phase, $Ca_c = 0.165$, $Re_c = 0.64$. **(a)**–**(b)** Squeezing stage; **(c)** Stretching stage; **(d)** Sub-droplet growth stage; **(e)** Snap-off stage.

and the morphological changes of the parent droplet. Therefore, the temporal evolution of the droplet elongation length is considered to be independent of the fluid density and the viscous properties of the solution. This phenomenon occurs because the droplet, when subjected to gravity, causes the necking region to deform in a manner similar to pure Newtonian behavior. Based on this assumption, we are able to accurately predict this phenomenon by adjusting the axial force balance originally proposed by Amsden. Based on our experimental findings, we observed that several forces play a role in the growth of the droplet elongation length. These forces include squeezing pressure, shear stress, and extensional stress, which are the main factors driving the droplet through the pore throat. Among them, the continuous phase liquid exerts viscous stresses with the purpose of thinning the neck. The proposed TAB model equations fully describe the deformation and rupture of the system.

We assumed that before the mother droplet deforms and the sub-droplet bursts, both the sub-droplet and the mother droplet are spherical and undeformed, as shown in Fig. 13.

The general equation for a damped force oscillator is:

$$m\frac{\mathrm{d}^2x}{\mathrm{d}t^2} = F_{\mathrm{ext}} - d\frac{\mathrm{d}x}{\mathrm{d}t} - kx \tag{7}$$

where x is the displacement of the droplet center of mass relative to its original undisturbed position. The following coefficients are taken from the Taylor analogy (Liu et al., 1993).

$$\frac{F_{\mathrm{ext}}}{m} = C_F\frac{\rho_c u_d^2}{\rho_d l_0} \tag{8}$$

$$\frac{k}{m} = C_k\frac{\sigma}{\rho_d l_0^3} \tag{9}$$

$$\frac{d}{m} = C_d\frac{\mu_d}{\rho_d l_0^2} \tag{10}$$

where u_d ($u_d = u_c$) is the relative velocity of the droplet, σ is the interfacial tension between the two phases, and C_F, C_k, C_d are dimensionless constants whose values are calculated experimentally (O'Rourke and Amsden, 1987). In the work based on Liu (Liu et al., 1993), the constant C_k was obtained by matching the fundamental frequency and derived $C_k = 8$. Based on the oscillation of the basic model, $C_d = 5$. In their experiments, (Liu et al., 1993)determined that the model predicts breakup if and only if $L > 1$, that is, $\frac{C_k C_b}{C_F} = 12$. ρ_c and ρ_d are the continuous and dispersed fluid densities, respectively. The model assumes that droplet breakup occurs if and only if $x > C_b l_0$, where C_b is an additional dimensionless constant. x is dimensioned by $C_b l_0$, such that $L = x\ C_b l_0$. Therefore, for the fundamental mode, the equatorial oscillation amplitude is half of the north-south amplitude. It is assumed that if the north-south oscillation amplitude is equal to the droplet radius, rupture will occur. This criterion yields $C_b = 1/2$ and $C_F = 1/3$. Therefore, Eq. (7) can be rewritten as:

$$\ddot{L} = \frac{C_F\rho_c u_d^2}{C_b} - C_k\frac{\sigma}{\rho_d l_0^3}L - C_d\frac{\mu_d}{\rho_d l_0^2}\dot{L} \tag{11}$$

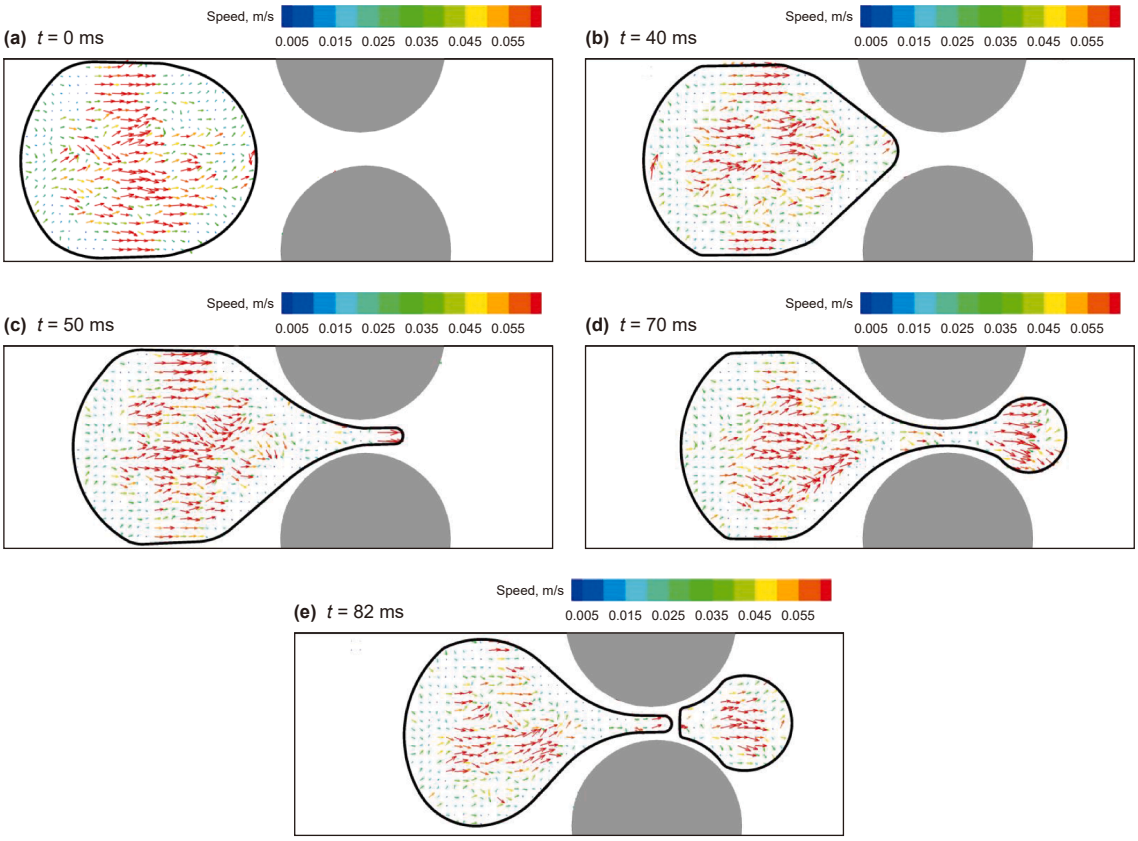

Fig. 12. Micro-PIV analysis of the velocity field distribution of the dispersed phase, $Ca_c = 0.384$, $Re_c = 1.1$. **(a)**–**(b)** Squeezing stage; **(c)** Stretching stage; **(d)** Sub-droplet growth stage; **(e)** Snap-off stage.

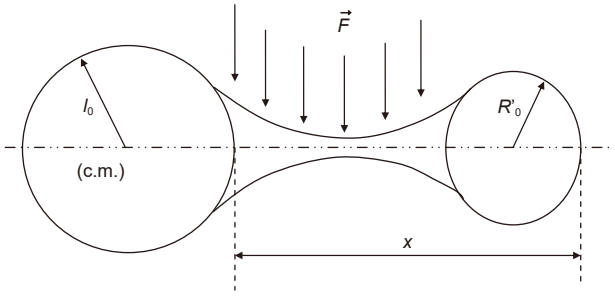

Fig. 13. TAB droplet deformation and rupture scene.

Breakup occurs if and only if $L > 1$. For a constant relative velocity $u_{d,}$ the solution to Eq. (11), i.e., the mother droplet elongation length is:

$$L(t) = \frac{We}{12} + e^{-\frac{t}{T}}\left[\left(l_0 - \frac{We}{12}\right)\cos\omega t + \frac{1}{\omega}\left(l_0 + \frac{l_0 - \frac{We}{12}}{t_d}\right)\sin\omega t\right] \tag{12}$$

where t_d is the theoretical breakup time for droplet deformation $t_d = \frac{5}{2}\frac{\mu_d}{\rho_d l_0^2}$; deformation factor $\omega = \frac{8\sigma}{\rho_d l_0^3}$. By solving this equation, we can determine the elongation size of the mother droplet and the critical size of the sub-droplet, at which point there is a critical elongation size. This occurs at a specific time when the mother droplet breaks and produces sub-droplet.

When the breakup cycle is reached, the critical elongation length of the mother droplet is obtained:

$$L(T) = \frac{We}{12} + e^{-1}\left[\left(l_0 - \frac{We}{12}\right)\cos\omega T + \frac{1}{\omega}\left(l_0 + \frac{l_0 - \frac{We}{12}}{t_d}\right)\sin\omega T\right] \tag{13}$$

The critical elongation length of the mother droplet is related to the different two-phase fluid properties. The critical elongation length values of the mother droplet with different fluid properties are calculated according to the above formula, as shown in Fig. 14(a) and (b). The error of the critical elongation length value of the mother droplet mainly comes from the acquisition error of the experimental data. In order to balance the critical length value under different Weber numbers, the critical characteristic length of the mother droplet $L(T) = 1.25$ and 1.6 is taken when predicting the particle size of the sub-droplet. Since the increase in the viscosity of the dispersed phase fluid makes the droplet have better ductility, the critical elongation length of the mother droplet in the experimental groups with different viscosities is slightly larger than that in the experimental groups with different interfacial tensions.

The energy of the mother droplet includes the minimum surface energy $\left(4\pi l_0^2\sigma\right)$ and the sum of the energy of oscillation and distortion $\left(E_{osc} = \frac{\pi}{5}\rho_c l_0^5\left[\left(\frac{dL}{dt}\right)^2 + \omega^2 L^2\right]\right)$. Considering other

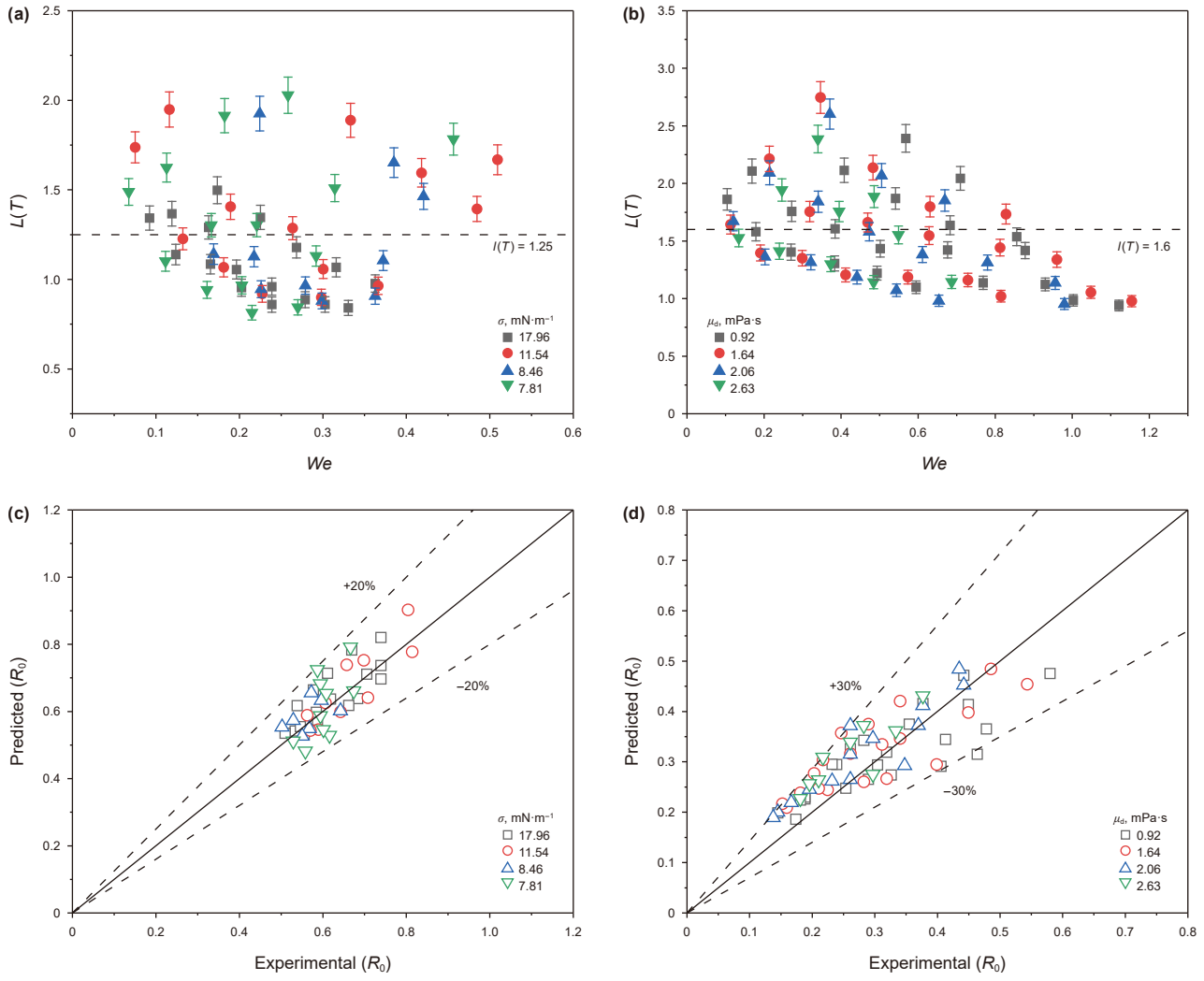

Fig. 14. **(a)**–**(b)** Critical elongation length of mother droplets with different fluid properties; **(c)**–**(d)** Comparison of experimental data and theoretical values of sub-droplet size with different fluid properties.

modes in the calculation of the mother droplet energy, the following equation can be obtained:

$$E_{\text{mother}} = 4\pi l_0^2\sigma + K\frac{\pi}{5}\rho_c l_0^5\left[\left(\frac{\mathrm{d}L}{\mathrm{d}t}\right)^2 + \omega^2 L^2\right] \tag{14}$$

where K is the ratio of the total energy of distortion and oscillation to the energy of the basic model. At the time of rupture, the sub-droplet is assumed to have no distortion and oscillation. Therefore, the energy after rupture is the sum of the minimum surface energy and kinetic energy of the sub-droplet. Since the velocity of the sub-droplet is normal to the flow direction of the mother droplet, the sub-droplet has kinetic energy. The energy in the sub-droplet is given by the following formula:

$$E_{\text{daughter}} = 4\pi l_0^2\sigma\frac{l_0}{R_0} + \frac{\pi}{6}\rho_c l_0^5 u_{\text{sum}}^2 \tag{15}$$

According to the law of conservation of energy, the total energy of the mother droplet before rupture is equal to the sum of the energy of the remaining droplet and the sub-droplet after rupture. The relationship between the initial length of the mother droplet l_0 and the particle size of the sub-droplet R_0 is obtained from Eqs. (9) and (10).

$$R_0 = \frac{l_0}{1 + \frac{8K(L(T))^2}{20} + \frac{\rho_c l_0^3 u_{\text{sum}}^2}{\sigma}\left(\frac{6K-5}{120}\right)} \tag{16}$$

The front cover radius when the droplet breaks is taken as the experimental value of the sub-droplet size, that is, the maximum value of R_H. In order to verify the effectiveness of the proposed semi-empirical model, the experimental and calculated values of the sub-droplet size of the experimental groups with different interfacial tensions and different viscosities are compared, as shown in Fig. 14(c) and (d). The predicted values of the sub-droplet size are in good agreement with the experimental values, and the prediction errors are within ±20% and ±30%. Since the Taylor analogy model is based on the Weber number (O'Rourke and Amsden, 1987) and is insensitive to changes in the viscosity of the droplet itself, the prediction effect of the sub-droplet size of the experimental groups with different viscosities is relatively poor.

4. Conclusion

This paper studied the influencing factors of the droplet deformation and fragmentation through a symmetric semi-

circular pore throat microchannel, by mean of experimental, then proposed a theoretical model to predict the size of the sub-droplet size at rupture time. A three-dimensional Particle Image Velocimetry technique was employed to visualize the passage of a droplet through the semi-circular pore throat geometry. The results revealed that the deformation of droplets in Newtonian flow involved four deformation stages: the squeezing, the stretching, the sub-droplet growth and the snap-off stages in chronological. The effects of interfacial tension, dispersed phase viscosity, pressure drop and micro-PIV analysis on droplet deformation and breakup were analyzed and we can conclude from our analysis that the interfacial tension, the fluid flow rates, the dispersed fluid concentration, the interfacial tension and the dispersed phase fluid viscosity significantly contribute in the droplet deformation and breakup process. Moreover, the pressure drops analysis of droplet breakup revealed that the squeezing effect of the continuous phase on the dispersed phase is the dominant factor in the growth of the sub-droplet. We successfully employed a Taylor-based model to predict the size of the sub-droplet formed at initial droplet breakup time. Based on our work, the predicted values of the sub-droplet size were in good agreement with the experimental values, and the prediction errors were within ±20% and ±30%. The prediction effect of the sub-droplet size of the experimental groups with different viscosities was relatively poor as the Taylor-based model is based on the Weber number and is insensitive to changes in the viscosity of the dispersed phase fluid.

CRediT authorship contribution statement

Yan Li: Writing – review & editing, Writing – original draft, Validation, Methodology, Data curation. **Yu-Qi Yang:** Writing – review & editing, Validation, Supervision, Resources, Project administration, Methodology, Funding acquisition, Conceptualization. **Essouma E. Ariane F.B.:** Validation, Project administration, Investigation. **Xiu-Fu Cheng:** Validation, Project administration, Investigation. **Hai-Peng Zhang:** Supervision, Resources, Project administration. **Zi-Zhen Wang:** Supervision, Project administration, Investigation. **Shu-Xing Mei:** Supervision, Project administration, Investigation. **Jian Liu:** Supervision, Resources, Project administration, Funding acquisition. **Yue-Qun Fu:** Supervision, Resources, Project administration. **Si-Yu Chen:** Supervision, Project administration.

Declaration of competing interest

The authors declare that they have no known competing financial interests or personal relationships that could have appeared to influence the work reported in this paper.

Acknowledgments

This research was funded by the National Natural Science Foundation of China (52574069), PetroChina Innovation Foundation (2024DQ02-0148), Central Guidance Fund for Local Science and Technology Development (ZYYD2023A08), Outstanding Youth Science Foundation of Xinjiang Uygur Autonomous Region (2025D01E65), Xinjiang Uygur Autonomous Region Tianshan Talent Project (2022TSYCCX0057) and Research Team Project for the Introduction of Strategic Talent under the 'One Matter, One Discussion' Policy in Xinjiang Uygur Autonomous Region (XZT3-3).

References

Abate, A.R., Mary, P., van Steijn, V., Weitz, D.A., 2012. Experimental validation of plugging during drop formation in a T-junction. Lab. Chip 12, 1516–1521. https://doi.org/10.1039/c2lc21263c.

de Haas, T.W., Fadaei, H., Guerrero, U., Sinton, D., 2013. Steam-on-a-chip for oil recovery: the role of alkaline additives in steam assisted gravity drainage. Lab. Chip 13. https://doi.org/10.1039/c3lc50612f.

Du, W., Fu, T., Duan, Y., Zhu, C., Ma, Y., Li, H.Z., 2018. Breakup dynamics for droplet formation in shear-thinning fluids in a flow-focusing device. Chem. Eng. Sci. 176, 66–76. https://doi.org/10.1016/j.ces.2017.10.019.

Duffy, D.C., McDonald, J.C., Schueller, O.J.A., Whitesides, G.M., 1998. Rapid prototyping of microfluidic systems in Poly(dimethylsiloxane). Anal. Chem. 70, 4974–4984. https://doi.org/10.1021/ac980656z.

Gao, W., Tang, X., Xu, M., Li, Y., Zhong, Y., Kong, D., Wen, Y., Li, Q., 2024. Surfactant–polymer viscosity effects on enhanced oil recovery across pore structures: microfluidic insights from pore scale to darcy scale. Energy Fuels. 38, 17380–17391. https://doi.org/10.1021/acs.energyfuels.4c02531.

He, L., Luo, Z., Bai, B.J.C.E.S., 2020. Breakup of pancake droplets flowing through a microfluidic constriction. Chem. Eng. Sci. 220, 115649. https://doi.org/10.1016/j.ces.2020.115649.

Huebner, A., Sharma, S., Srisa-Art, M., Hollfelder, F., Edel, J.B., Demello, A.J.J.L.o.a.C., 2008. Microdroplets: a sea of applications? Lab. Chip 8, 1244–1254. https://doi.org/10.1039/B806405A.

Li, L., Zhang, D., Su, Y., Hao, Y., Zhang, X., Huang, Z., Zhang, W.J.P.o.F., 2024. Investigation of oil/water two-phase flow behavior in laminated shale porous media considering heterogeneous structure and fluid-solid interaction. Phys. Fluids 36, 033315. https://doi.org/10.1063/5.0192714.

Li, Z., Gu, Z., Li, R., Wang, C., Chen, C., Yu, C., Zhang, Y., Shu, Q., Su, J.J.C.E.S., 2021. Investigation on droplet dynamic snap-off process in a short, abrupt constriction. Chem. Eng. Sci. 235, 116496. https://doi.org/10.1016/j.ces.2021.116496.

Li, Z., Xu, D., Yuan, Y., Wu, H., Hou, J., Kang, W., Bai, B., 2020. Advances of spontaneous emulsification and its important applications in enhanced oil recovery process. Adv. Colloid Interface Sci. 277. https://doi.org/10.1016/j.cis.2020.102119.

Liang, X., Wang, X., Lu, S., Wang, K., Luo, G., 2021. Pressure drop analysis for the droplet break-up flow in a locally constrictive microchannel. Chem. Eng. Sci. 230, 116190. https://doi.org/10.1016/j.ces.2020.116190.

Lifton, V.A., 2016. Microfluidics: an enabling screening technology for enhanced oil recovery (EOR). Lab. Chip 16, 1777–1796. https://doi.org/10.1039/c6lc00318d.

Liu, A.B., Mather, D., Reitz, R.D.J.S.T., 1993. Modeling the effects of drop drag and breakup on fuel sprays. SAE Tech. Pap, 930072. https://doi.org/10.4271/930072.

Ma, S., Sherwood, J.M., Huck, W.T.S., Balabani, S., 2015. The microenvironment of double emulsions in rectangular microchannels. Lab. Chip 15, 2327–2334. https://doi.org/10.1039/c5lc00346f.

McDonald, J.C., Duffy, D.C., Anderson, J.R., Chiu, D.T., Wu, H., Schueller, O.J.A., Whitesides, G.M., 2000. Fabrication of microfluidic systems in Poly(-dimethylsiloxane). Electrophoresis 21, 27–40. https://doi.org/10.1002/(SICI)1522-2683(20000101)21:1<27::AID-ELPS27>3.0.CO;2-C.

Nan, L., Zhang, H., Weitz, D.A., Shum, H.C., 2024. Development and future of droplet microfluidics. Lab. Chip 24, 1135–1153. https://doi.org/10.1039/d3lc00729d.

Nghe, P., Tabeling, P., Ajdari, A., 2010. Flow-induced polymer degradation probed by a high throughput microfluidic set-up. J. Non-Newtonian Fluid Mech. 165, 313–322. https://doi.org/10.1016/j.jnnfm.2010.01.006.

O'Rourke, P.J., Amsden, A.A., 1987. The TAB method for numerical calculation of spray droplet breakup. SAE Tech. Pap, 872089.

Palizdan, S., Abbasi, J., Riazi, M., Malayeri, M.R., 2020. Impact of solutal Marangoni convection on oil recovery during chemical flooding. Pet. Sci. 17, 1298–1317. https://doi.org/10.1007/s12182-020-00451-z.

Perazzo, A., Tomaiuolo, G., Preziosi, V., Guido, S., 2018. Emulsions in porous media: from single droplet behavior to applications for oil recovery. Adv. Colloid Interf. Sci. 256, 305–325. https://doi.org/10.1016/j.cis.2018.03.002.

Quennouz, N., Ryba, M., Argillier, J.-F., Herzhaft, B., Peysson, Y., Pannacci, N.J.O., Science, G., nouvelles, T.R.d.I.E., 2014. Microfluidic study of foams flow for enhanced oil recovery (EOR). Oil Gas Sci. Technol. 69, 457–466. https://doi.org/10.2516/ogst/2014017.

Roof, J., 1970. Snap-off of oil droplets in water-wet pores. Soc. Petrol. Eng. J. 10, 85–90. https://doi.org/10.2118/2504-PA.

Rossen, W.R.J.C., Physicochemical, S.A., Aspects, E., 2000. Snap-off in constricted tubes and porous media. Colloid Surf. A-Physicochem. Eng. Asp. 166, 101–107. https://doi.org/10.1016/s0927-7757(99)00408-2.

Singla, A., Mehul, B., Ray, B., 2024. Droplet dynamics in a constricted microchannel. Chem. Eng. Sci. 300. https://doi.org/10.1016/j.ces.2024.120532.

Stone, H.A., 2005. On lubrication flows in geometries with zero local curvature. Chem. Eng. Sci. 60, 4838–4845. https://doi.org/10.1016/j.ces.2005.03.021.

Tsai, T., Miksis, M.J.J.J.o.f.m., 1994. Dynamics of a drop in a constricted capillary tube. J. Fluid Mech. 274, 197–217.

Wang, K., You, Q., Long, Q.M., Zhou, B., Wang, P., 2023. Experimental study of the mechanism of nanofluid in enhancing the oil recovery in low permeability reservoirs using microfluidics. Pet. Sci. 20, 382–395. https://doi.org/10.1016/j.petsci.2022.09.026.

Wang, X.D., Liu, Y.Y., Liu, D.Y., Ge, X.H., Li, L., Qiu, T., 2022. Droplet breakup in the square microchannel with a short square constriction to generate slug flow. AIChE J. 68, e17739. https://doi.org/10.1002/aic.17739.

Wang, K., Luo, G., Yang, C., 2014. Droplet generation in microfluidic systems with double-loop feedback control. Lab. Chip 14 (13), 2259–2267.

Wong, H., Radke, C.J., Morris, S., 1995. The motion of long bubbles in polygonal capillaries. Part 1. Thin films. J. Fluid Mech. 292, 71–94. https://doi.org/10.1017/S0022112095001443.

Yao, C., Zhao, Y., Ma, H., Liu, Y., Zhao, Q., Chen, G., 2021. Two-phase flow and mass transfer in microchannels: a review from local mechanism to global models. Chem. Eng. Sci. 229, 116017. https://doi.org/10.1016/j.ces.2020.116017.

Zhao, X.Z., Liao, G.Z., Gong, L.Y., Luan, H.X., Chen, Q.S., Liu, W.D., Liu, D., Feng, Y.J., 2022. New insights into the mechanism of surfactant enhanced oil recovery: micellar solubilization and in-situ emulsification. Pet. Sci. 19, 870–881. https://doi.org/10.1016/j.petsci.2021.11.014.

Zhou, J., Ellis, A.V., Voelcker, N.H., 2010. Recent developments in PDMS surface modification for microfluidic devices. Electrophoresis 31, 2–16. https://doi.org/10.1002/elps.200900475.

Zou, X., Luo, W., Chang, Z., Wang, X., 2024. Critical criterion for droplet breakup in a contractive microchannel. Exp. Therm. Fluid Sci. 150. https://doi.org/10.1016/j.expthermflusci.2023.111034.